Journal of Functional Materials and Applied Engineering

Research Paper

Self-assembly synthesis of CdSrGO composite aerogels and its photocatalytic degradation of tetracycline hydrochloride

Carlos Mendez[1], Priya Patel[1,*]

[1] Faculty of life science, Universitas Indonesia (UI), Depok City, Indonesia and Asia Pacific University of Technology and Innovation (APU), Technology Park, Malaysia
*Corresponding author: Mendez_life@gmail.com; Patel_life@yahoo.com

Abstract. A CdS/reduced graphene oxide (rGO) composite aerogel with CdS nanosheets (CdS NSs) grown on an interconnected three-dimensional rGO-based porous network was prepared by a one-pot hydrothermal method using L-lysine as the reducing agent and cross-linker. The results show that its enhanced adsorption toward pollutants, owing to its large Brunauer-Emmett-Teller (BET) specific surface area and spongy nature, combined with improved light absorption due to its extremely lightweight character, contributes to superior performance. Moreover, the incorporation of rGO promotes the separation of photogenerated charge carriers. Thus, the CdS/rGO composite aerogel exhibits markedly enhanced activity for photocatalytic degradation. It can be observed that tetracycline hydrochloride (TC) is totally degraded after 45 min of irradiation with the CdS/rGO composite aerogel, and almost all TC is mineralized after 1.5 h. Furthermore, the CdS/rGO composite aerogel demonstrates high stability and can be readily separated from the reaction system for recycling. The photocatalytic activity of the CdS/rGO composite aerogel shows no obvious decrease after five consecutive cycles.

Keywords: *RGO aerogel; CdS; photocatalysis; tetracycline hydrochloride; recycle*

Received on 02 June 2025, Accepted on 02 August 2025, Published on 15 September 2025

1 Introduction

Cadmium sulfide (CdS) is a photocatalytic material responsive to visible light [1−4]. However, its tendency to agglomerate, poor stability, and susceptibility to photocorrosion severely limit its practical applicability. Consequently, modifying the crystal phase structure, morphology, and size of CdS, as well as suppressing the recombination of photogenerated carriers, significantly impacts its photocatalytic activity. Studies indicate that interfaces between CdS nanoparticles are prone to agglomeration, whereas CdS nanosheets (CdS NSs) generally exhibit a higher degree of crystallinity compared to nanoparticles. This reduces carrier recombination centers arising from crystal defects and endows the crystals with superior carrier mobility [5]. In recent years, solvothermal methods have been employed to synthesize CdS NSs; however, these processes utilize high-temperature organic solvents, which not only increase synthesis costs but also cause severe environmental pollution. Furthermore, CdS powder tends to settle at the bottom of water bodies, resulting in low light utilization efficiency and difficulties in post-use recovery, thereby restricting its application. Therefore, harnessing the high-efficiency photocatalytic performance of CdS while circumventing its inherent drawbacks remains a formidable challenge. To address these issues, immobilizing CdS onto various heterogeneous catalytic supports, such as carbon materials, polymers, and metal oxides[9−12], is a common strategy to preserve its activity and longevity.

Carbon-based materials, including fullerenes, carbon nanotubes, and graphene, serve as excellent supports for nanomaterials in heterogeneous catalysis[13−15]. Among them, reduced graphene oxide (rGO) possesses a large specific surface area and ultra-high electrical conductivity, which facilitate the separation of photogenerated electrons and holes, thereby enhancing the photocatalytic performance of nanomaterials[16−20]. Additionally,

rGO aerogels retain all the advantageous properties of rGO nanosheets while offering superior mechanical strength, easy recyclability, and an extremely low density that allows them to float on water surfaces to harvest more sunlight[21−22]. These exceptional traits render rGO aerogels ideal supports for nanomaterials. Currently, composites featuring CdS loaded on two-dimensional rGO sheets have been extensively studied[23−25], yet the inconvenient recovery and reuse of two-dimensional catalysts limit their practical deployment. Conversely, research on the preparation and photocatalytic performance of three-dimensional (3D) CdS/rGO composite aerogels with practical application value remains insufficient.

In this work, CdS NSs were anchored onto an rGO aerogel matrix via a facile hydrothermal method to fabricate a CdS/rGO composite aerogel, and its performance in the photocatalytic degradation of TC was systematically investigated. Compared to pristine CdS, which suffers from severe agglomeration and difficult recovery, the CdS/rGO composite aerogel achieves highly efficient photocatalytic degradation of aqueous TC and exhibits excellent photocatalytic stability. Embedding CdS NSs within the rGO aerogel matrix paves a novel pathway for designing efficient photocatalysts with tangible practical value.

2 Experimental Materials and Methods

2.1 Raw Materials

Natural flake graphite (99.99%, 300 mesh) was supplied by Alfa Aesar. L-lysine (analytical reagent, AR) and cadmium acetate ($Cd(Ac)_2$, AR) were purchased from Aladdin Reagent Co., Ltd. Thiourea (AR), sodium nitrate ($NaNO_3$, AR), potassium permanganate ($KMnO_4$, AR), 98% sulfuric acid (H_2SO_4, AR), and 30% hydrogen peroxide (H_2O_2, AR) were obtained from Sinopharm Chemical Reagent Co., Ltd.

2.2 Preparation of Graphene Oxide (GO)

GO was synthesized from natural flake graphite using a modified Hummers method [20]. The detailed procedure is as follows: Initially, 10 g of natural flake graphite was added to a 2 L beaker. Under an ice-water bath, 5 g of $NaNO_3$ and 160 mL of 98% H_2SO_4 were introduced. Subsequently, 25 g of $KMnO_4$ was slowly added to the mixture while maintaining the temperature below 20 °C. After stirring at room temperature for 10 h, 600 mL of deionized water was added, and the reaction temperature was controlled at approximately 98 °C. Stirring continued for 2 h before a large volume of deionized water was added to terminate the reaction. Concurrently, 25 mL of 30% H_2O_2 solution was introduced to reduce excess $KMnO_4$ until bubble generation ceased, at which point the solution turned from dark brown-black to a bright yellow. The mixture was hot-filtered, and the solid product was washed with dilute hydrochloric acid (2 L, 1:10 volume ratio). Washing with deionized water was repeated until no sulfate ions were detected in the filtrate (tested with $BaCl_2$ solution). Finally, the product was centrifuged at 10,000 r/min for 30 min to obtain a solid precipitate. After multiple washing and centrifugation cycles, the resultant product was ultrasonicated for 30 min and redispersed in water to yield a GO sol (5 mg/mL).

2.3 Preparation of Photocatalysts

A predetermined amount of GO (20 mL, 5 mg/mL) was ultrasonically dispersed in 50 mL of deionized water. Subsequently, 200 mg of L-lysine was added and dissolved completely, followed by ultrasonication for 30 min. Appropriate amounts of $Cd(Ac)_2$ and thiourea were then introduced. The mixed solution was transferred into a 100 mL Teflon-lined autoclave and maintained at 160 °C for 10 h, followed by natural cooling to room temperature. The resulting CdS/rGO composite hydrogel was dialyzed extensively with deionized water and then subjected to freeze-drying to obtain the 3D CdS/rGO composite aerogel. For comparison, CdS powder was synthesized under identical conditions without the addition of GO dispersion.

2.4 Catalyst Characterization

The crystal phase structure was analyzed using a Bruker D8 Advance X-ray powder diffractometer (XRD) with Cu Kα radiation (λ = 0.15406 nm), operating at 40 kV and 40 mA. Raman spectra were acquired using an invia-Reflex Micro-Raman Spectroscopy system equipped with an Ar-ion laser providing 532 nm monochromatic light. Transmission electron microscopy (TEM) was performed on a Tecnai 20 FEG microscope to observe the morphology, size, dispersion, and particle size distribution of the nanoparticles. Samples were dispersed in

ethanol at a specific ratio, ultrasonicated to ensure homogeneity, drop-cast onto carbon-coated copper grids, and dried prior to observation. Surface morphology and particle size were characterized using a JSM-6700F field-emission scanning electron microscope (SEM) with an accelerating voltage of 5–30 kV and a chamber vacuum better than 2.7×10^{-5} Pa. Fourier-transform infrared (FT-IR) spectra were recorded on a Nicolet Nexus 670 FTIR spectrometer using the KBr pellet transmission method. Specific surface area measurements were conducted on an ASAP 2020 automatic physical and chemical adsorption apparatus. Nitrogen adsorption-desorption isotherms were collected at 77 K (liquid nitrogen temperature). Samples were degassed at 120 °C for 4 h prior to analysis. The specific surface area was calculated via the multipoint BET method based on adsorption data within the relative pressure range (P/P_o = 0.00–0.35), and the Barrett-Joyner-Halenda (BJH) method was employed to analyze pore size distribution. X-ray photoelectron spectroscopy (XPS) was performed on a Quantum 2000 spectrometer using a monochromatized Al Kα X-ray source (energy = 1486.6 eV). During analysis, the X-ray spot size was 100 µm, and the power was set to 25 W. The C 1s binding energy at 284.8 eV was used as the calibration reference. Total organic carbon (TOC) content was analyzed using a TOC-V (CPH) analyzer. The electrical conductivity of the samples was determined by measuring the resistivity (Ω·cm) of a unit volume (1 cm × 1 cm × 1 cm) using the four-probe method.

2.5 Photocatalytic Performance Evaluation

The photocatalytic activity of the prepared CdS/rGO composite aerogel was evaluated using TC as the target pollutant under visible light irradiation. The experimental procedure was as follows: The CdS/rGO composite aerogel was added to 60 mL of a TC solution (50 mg/L). A 300 W xenon lamp equipped with a 420 nm cutoff filter served as the light source, providing an irradiance of 0.35 W/cm² at the sample surface. At predetermined time intervals, 4.0 mL of the reaction suspension was sampled and analyzed using ultraviolet-visible (UV-Vis) spectroscopy. The concentration change of TC during degradation was determined by monitoring the absorbance at its maximum absorption wavelength (356 nm). The degradation efficiency was expressed as C/C0, where Cis the concentration at a given sampling time and C0 is the initial concentration of TC.

3 Results and Discussion

3.1 Characterization of CdS/rGO Composite Aerogel

Utilizing L-lysine as both the reducing agent and cross-linker, and employing GO, $Cd(Ac)_2$, and thiourea as precursors, a CdS/rGO composite hydrogel was successfully synthesized via a facile hydrothermal method. Previous studies indicated that the optimal mass ratio of GO to L-lysine (R

G/L) for forming lys-rGO hydrogels is 1:2[26]. Therefore, this ratio was fixed, and the influence of the GO to $Cd(Ac)_2$ mass ratio (RG/C=1:1to 1:5) on hydrogel formation was investigated. Fig. 1 presents photographs of CdS/rGO composite hydrogels synthesized with varying $Cd(Ac)_2$ contents. Three-dimensional cylindrical hydrogels conforming to the shape of the reaction vessel were obtained across the entire RG/C range tested, with negligible volume variation relative to changes in RG/C . For instance, at RG/C =1:5, the resulting cylindrical hydrogel exhibited a diameter of approximately 20 mm and a height of about 30 mm.

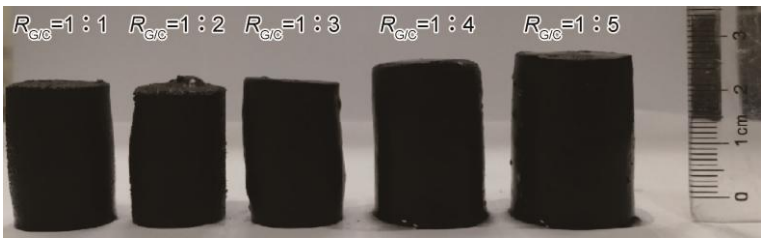

Figure 1 Photographs of CdS/rGO composite hydrogels with different amounts of $Cd(Ac)_2$.

The appearance of the CdS/rGO composite hydrogel and the corresponding aerogel obtained after freeze-drying dehydration is shown in Fig. 2(a). It is evident that the volume remained largely unchanged after the phase transition. The CdS/rGO composite aerogel prepared at RG/C =1:4was selected as a representative sample for

further microstructural observation via SEM and TEM. The SEM image of the CdS/rGO composite aerogel (Fig. 2(b)) reveals a typical interconnected porous architecture, with a large quantity of nanoscale materials uniformly anchored on the rGO sheet surfaces. For comparison, CdS powder synthesized under identical conditions but without GO addition was examined. The SEM image of the CdS powder (Fig. 2(b)) clearly shows severe agglomeration, demonstrating that the introduction of GO provides a high specific surface area that effectively disperses the material and prevents CdS aggregation. The TEM image of the CdS/rGO composite aerogel (Fig. 2(c)) further confirms the unique interconnected lamellar porous nanostructure, wherein abundant nanosheet-like substances are homogeneously dispersed across the rGO sheets. The high-resolution TEM (HRTEM) image (inset in Fig. 2(c)) displays distinct lattice fringes with a spacing of d=0.335nm, corresponding to the (002) plane of hexagonal CdS. This confirms that the nanosheet-like substance is CdS and has been successfully loaded onto the rGO sheets. The size distribution of the supported CdS NSs is presented in Fig. 2(d), indicating that the CdS NSs range from 10 to 40 nm in size, with an average dimension of 25 nm.

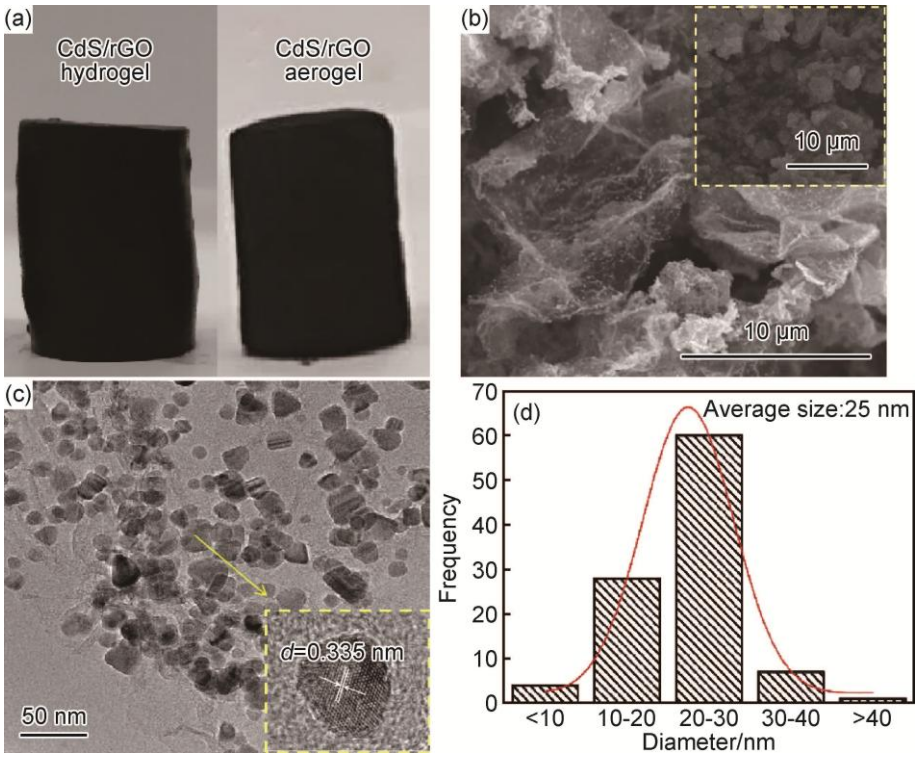

Figure 2 Photograph and microstructure of CdS/rGO composite aerogel. (a) Photograph; (b) SEM image; (c) TEM image; (d) Size distribution of supported CdS NSs.

The XRD pattern of the CdS/rGO composite aerogel is displayed in Fig. 3(a). Characteristic diffraction peaks are observed at 2θ=24.8◦, 26.5◦, 28.2◦, 43.7◦, 47.9◦, and 51.8◦, which are assignable to the (100), (002), (101), (110), (103), and (112) crystal planes of hexagonal-phase CdS (JCPDF 01-070-2553), respectively. This further verifies the successful loading of CdS NSs onto the rGO aerogel matrix. However, the diffraction peak for the (002) crystal plane of rGO, typically expected around 2θ=24.3◦, is not prominent in the XRD pattern. Therefore, FT-IR spectroscopy was employed to assess the reduction degree of GO. Compared to pristine GO, the FT-IR spectrum of the CdS/rGO composite aerogel (Fig. 3(b)) shows a significant attenuation of absorption peaks at 1720 cm^{-1} and 3300 cm^{-1}, indicating the reduction of most carbonyl and hydroxyl groups on the GO surface during the formation of the composite aerogel. Furthermore, the reduction degree of GO is corroborated by XPS analysis (Fig. 3(c)). The C 1s XPS spectrum of the CdS/rGO composite aerogel reveals that the O–C content is 20.8%, a drastic decrease from 55% in pristine GO. This substantial reduction in O–C content signifies that GO has been highly reduced to rGO during the hydrothermal gelation process. This value is comparable to the O–C content (21.8%) observed in our previously reported lys-rGO aerogel[26], implying that the rGO within the prepared CdS/rGO composite aerogel maintains a high degree of reduction. The Raman spectra of CdS/rGO composite aerogel, GO, and rGO are presented in Fig. 3(d). In the Raman spectrum of GO, two characteristic

peaks appear at 1565 cm^{-1} and 1321 cm^{-1}, assigned to the G band (graphitic sp2-bonded carbon) and the D band (sp2carbon breathing mode), respectively. For the lys-rGO aerogel and the CdS/rGO composite aerogel, both the D and G bands shift to higher wavenumbers (1346 cm^{-1} and 1594 cm^{-1}). Concurrently, the intensity ratio of the D band to the G band (ID /IG) for the CdS/rGO composite aerogel is 1.03, slightly higher than the ratio of 0.96 observed for GO. This increase suggests the introduction of surface defects during the formation of the CdS/rGO composite aerogel. Notably, the CdS/rGO composite aerogel and the rGO aerogel possess nearly equivalent O–C contents and ID /IGratios (the latter being 1.01 for rGO aerogel). These findings indicate that the incorporation of CdS NSs does not exacerbate the basal plane defects of the rGO aerogel matrix [27–28]. Collectively, all structural characterizations confirm the successful preparation of the CdS/rGO composite aerogel.

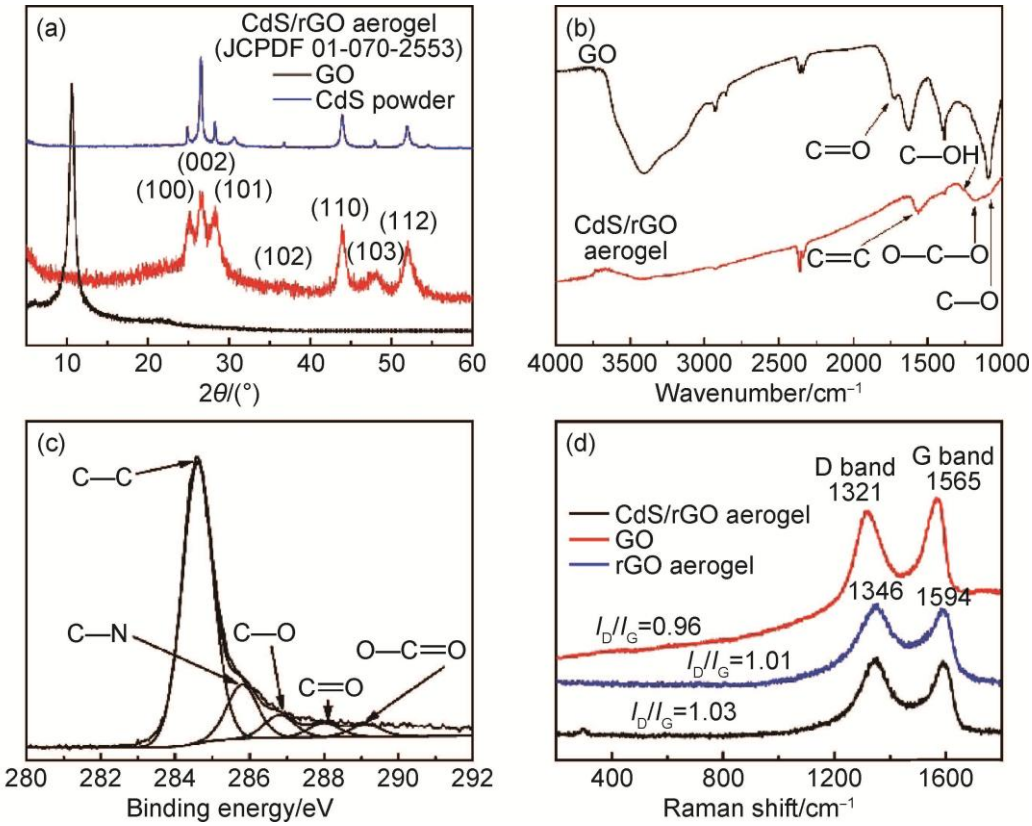

Figure 3 Structural characterization of CdS/rGO composite aerogel. (a) XRD pattern; (b) FT-IR spectra; (c) XPS spectra; (d) Raman spectra.

3.2 Formation Process of CdS/rGO Composite Aerogel

Our previous research demonstrated that electrostatic attraction and hydrogen bonding exist between L-lysine and GO, alongside π-π stacking interactions between GO nanosheets. Consequently, under hydrothermal conditions, GO nanosheets cross-link and gelate to form a 3D lys-rGO hydrogel[26]. Building upon this foundation, the formation mechanism of the CdS/rGO composite aerogel is proposed, as illustrated in Fig. 4. L-lysine, a basic amino acid, yields a mixed solution with GO at a pH of approximately 10.8. At this pH, L-lysine predominantly exists as a zwitterion with deprotonated carboxyl groups and protonated amino groups. The protonated amino groups of L-lysine are electrostatically adsorbed onto the GO surface, exposing the deprotonated carboxyl groups outward. Subsequently, $Cd(Ac)_2$ and thiourea are introduced into the mixture. Owing to electrostatic attraction, the pendant deprotonated carboxyl groups of L-lysine act as anchoring sites for Cd^{2+} ions. During the hydrothermal process, GO is reduced to rGO and undergoes π-π stacking-driven self-assembly to form the hydrogel network. Simultaneously, uniformly sized CdS NSs are generated and homogeneously dispersed on the surfaces of the rGO nanosheets. Ultimately, the jelly-like composite hydrogel is directly dehydrated via freeze-drying to yield the CdS/rGO composite aerogel.

DOI:

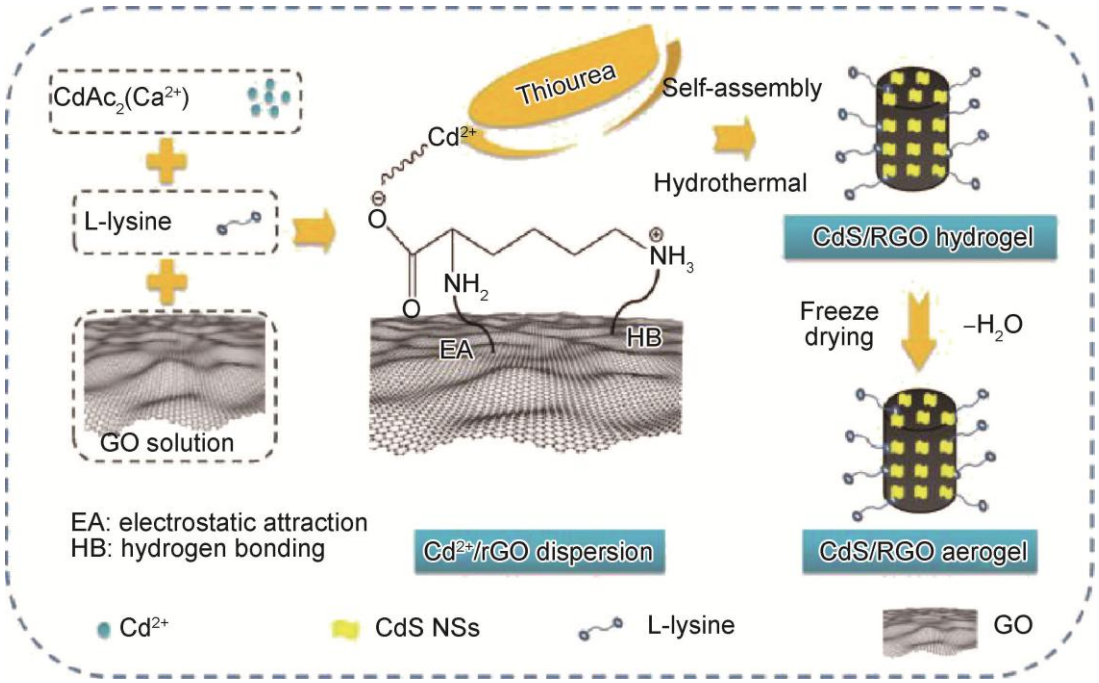

Figure 4 Schematic illustration of the formation of CdS/rGO composite hydrogel and the corresponding aerogel.

3.3 Mechanical Properties of CdS/rGO Composite Aerogel

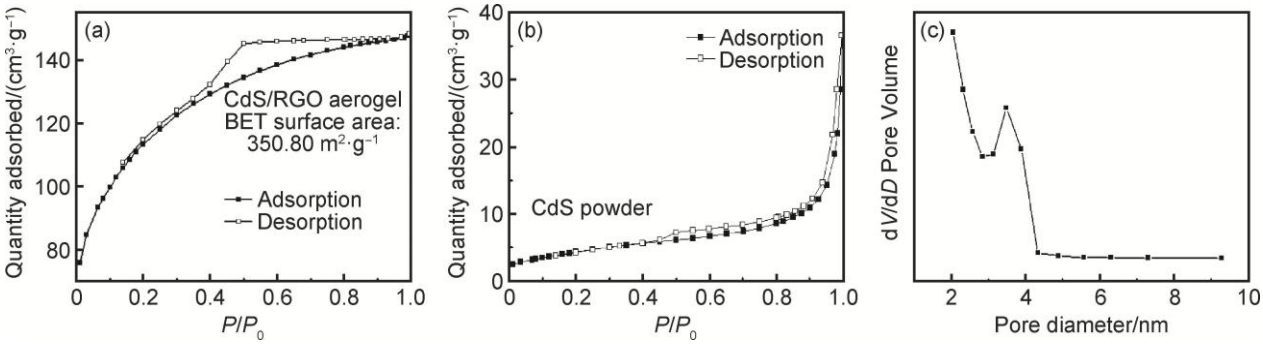

Figure 5 Nitrogen adsorption-desorption isotherms of CdS/rGO composite aerogel (a) and CdS powder (b), and pore size distribution profile of CdS/rGO composite aerogel (c).

Our earlier prepared lys-rGO aerogel suffered from poor thermal stability under vacuum and failed to yield an effective BET specific surface area[26]. In contrast, the N_2 adsorption-desorption isotherm of the CdS/rGO composite aerogel (Fig. 5(a)) demonstrates that embedding CdS NSs significantly enhances its thermal stability and increases the BET specific surface area to 350.80 m^2/g. Comparing the N_2 adsorption-desorption isotherms of the CdS/rGO composite aerogel (Fig. 5(a)) and pristine CdS powder (Fig. 5(b)) reveals that the composite aerogel possesses a vastly larger BET specific surface area than CdS powder (15.76 m^2/g) synthesized under identical conditions. This can be attributed to the fact that the embedded CdS NSs act as spacers between rGO nanosheets, effectively preventing their aggregation and restacking. Simultaneously, the rGO sheets facilitate the formation of smaller, more uniformly dispersed CdS NSs. As shown in Fig. 5(c), the BJH average pore diameter of the CdS/rGO composite aerogel is 3.6 nm, indicative of an ordered mesoporous structure. This further confirms that the insertion of CdS NSs between rGO sheets effectively inhibits rGO stacking. Compared to the lys-rGO aerogel, the dispersion of rGO nanosheets within this composite aerogel is markedly improved, a finding consistent with the SEM observations (Fig. 2(b)). The compressive performance of the CdS/rGO composite aerogel was also evaluated. As depicted in Fig. 6, the CdS/rGO composite aerogel can support a load exceeding 530 times its own weight without significant deformation, a figure far surpassing the compressive

performance of lys-rGO aerogel. This indicates that the incorporation of CdS NSs substantially reinforces the mechanical strength of the rGO aerogel.

Figure 6 Load-bearing abilities of CdS/rGO composite aerogel.

3.4 Photocatalytic Performance of CdS/rGO Composite Aerogel

The UV/Vis diffuse reflectance spectra (DRS) of the CdS/rGO composite aerogel and CdS powder are presented in Fig. 7. The bandgap of pristine CdS is approximately 2.36 eV. Upon loading CdS onto rGO, the resulting CdS/rGO composite aerogel exhibits a broadened light absorption range in the visible region[29−30]. Moreover, the CdS/rGO composite aerogel possesses an ultra-low density of 0.01 g/cm³. Unlike CdS powder, which readily settles to the bottom of water, the composite aerogel floats on the water surface, thereby harvesting more sunlight. This characteristic highlights its significant potential for practical applications in photocatalytic water pollutant remediation.

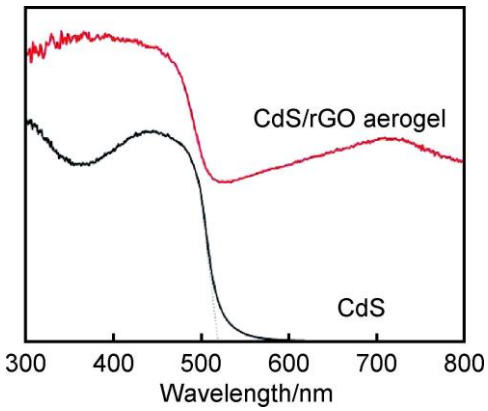

Figure 7 UV/Vis DRS spectra of CdS/rGO aerogel and powder CdS.

Consequently, the photocatalytic degradation performances of the CdS/rGO composite aerogel and CdS powder toward TC under visible light irradiation were investigated. The degradation efficiency can be evaluated by monitoring the temporal evolution of the UV-Vis absorption spectrum of TC, specifically the absorbance at its primary peak (356 nm). Fig. 8(a) shows the UV-Vis absorption spectral changes of the TC solution over time when using the CdS/rGO composite aerogel as the photocatalyst under visible light irradiation. The absorbance of the primary peak at 356 nm gradually diminishes, and a blueshift of the absorption peak at 275 nm is observed. These results indicate the decomposition of the TC backbone and the generation of derivative intermediates[31−32]. After 45 min of visible light irradiation, the peaks corresponding to TC and its derivatives nearly vanish, suggesting the breakdown of TC into small organic molecules or CO_2. After 1.5 h of reaction, the TOC removal rate reached 88.9%, further confirming the mineralization of the majority of TC. In contrast, the degradation efficiency of TC using CdS powder as the photocatalyst is presented in Fig. 8(b). Only 63% of TC conversion is achieved after 45 min of visible light irradiation, and the TOC removal rate is a mere 23.8% after

1.5 h, significantly lower than that of the composite aerogel. Meanwhile, the photodegradation of TC in the absence of any photocatalyst is negligible (Fig. 8(c)).

The superior photocatalytic performance of the CdS/rGO composite aerogel over CdS powder can be ascribed to four synergistic factors: (1) Compared to CdS powder, the CdS/rGO composite aerogel possesses a significantly larger BET specific surface area and a spongy texture, enabling the adsorption of substantial amounts of TC onto active sites—a prerequisite for efficient photocatalytic degradation. Fig. 8(d) illustrates the adsorption capacities of the CdS/rGO composite aerogel and CdS powder for TC under dark conditions. It is evident that 48% of TC can be adsorbed onto the surface of the composite aerogel, whereas only 0.9% adsorbs onto CdS powder. (2) In contrast to sedimented CdS powder, the CdS/rGO composite aerogel features an interconnected porous structure and an extremely low density (0.01 g/cm³), allowing it to float on water surfaces and absorb more visible light. (3) The high crystallinity of CdS NSs reduces carrier recombination centers originating from crystal defects, endowing the material with superior carrier mobility. (4) The incorporation of rGO facilitates the separation of photogenerated electrons and holes, mitigates photocorrosion on the CdS surface, and thereby enhances photocatalytic performance. Additionally, the CdS/rGO composite aerogel maintains a relatively high electrical conductivity (11.92 S/m).

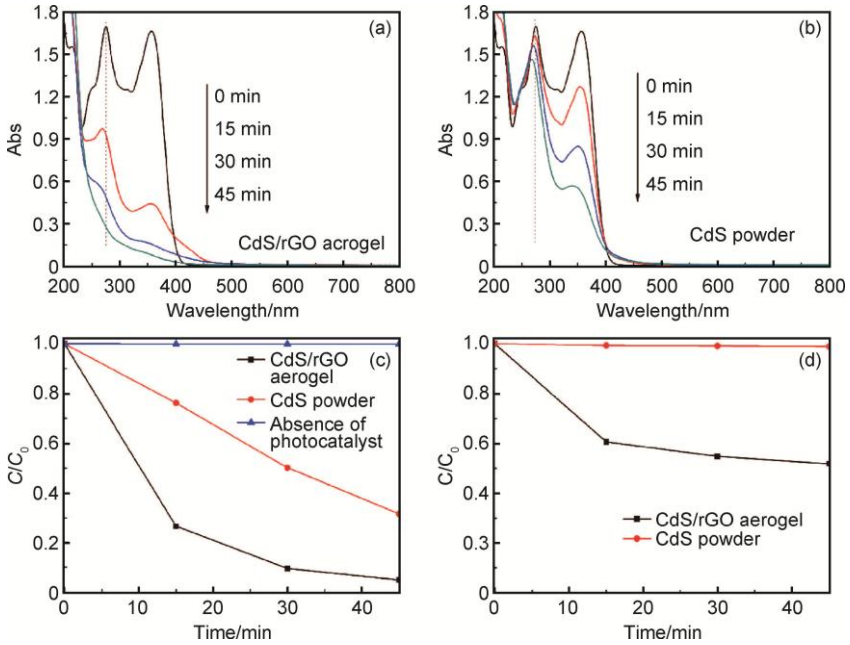

Figure 8 Photocatalytic degradation of TC: (a) CdS/rGO aerogel; (b) CdS powder; (c) Comparison under irradiation and in dark conditions; (d) Dark adsorption profiles of CdS/rGO aerogel and CdS powder.

3.5 Stability Test of CdS/rGO Composite Aerogel

The cycling stability of the CdS/rGO composite aerogel and CdS powder was evaluated, as shown in Fig. 9. After the photocatalytic reaction, the CdS/rGO composite aerogel can be readily retrieved using tweezers without any catalyst loss (Fig. 9(a)). Fig. 9(b) compares the photocatalytic activities over five successive cycles. The photocatalytic activity of the CdS/rGO composite aerogel shows no marked decline (black line in Fig. 9(b)). Conversely, CdS powder is susceptible to photocorrosion during the photocatalytic reaction, and unavoidable losses occur during its separation and recovery. After five cycles, the photocatalytic activity of CdS powder retains only 51% of its initial value (green line in Fig. 9(b)). Evidently, beyond its excellent photocatalytic performance, the CdS/rGO composite aerogel exhibits outstanding cycling stability, a crucial attribute for practical applications.

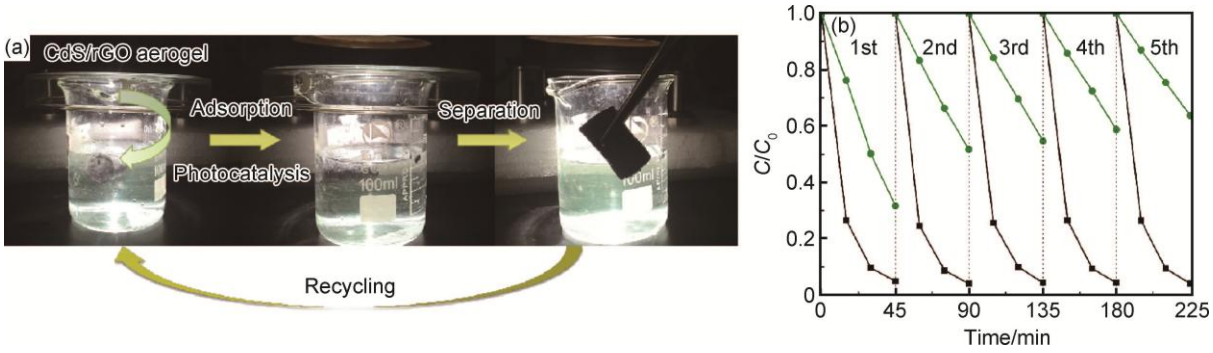

Figure 9 Photodegradation and recycling process of CdS/rGO composite aerogel: (a) Schematic of recycling; (b) Comparison of cycling runs for CdS/rGO aerogel and CdS powder.

The exceptional photocatalytic performance of the CdS/rGO composite aerogel toward tetracycline hydrochloride (TC) degradation arises from a sophisticated interplay of structural architecture, interfacial electronic modulation, and reaction engineering advantages, which collectively overcome the intrinsic limitations of pristine CdS nanoparticles. The formation mechanism initiates with the molecular-level mediation of L-lysine, which serves dual roles as a reducing agent and a cross-linking template. Under hydrothermal conditions, the alkaline environment (pH ~10.8) renders L-lysine as a zwitterion: its protonated amino groups ($-NH_3^+$) establish strong electrostatic attractions with the negatively charged oxygen-containing functional groups (e.g., -COOH, -OH) on graphene oxide (GO) surfaces, while the exposed deprotonated carboxyl groups ($-COO^-$) act as spatially confined nucleation sites for Cd^{2+} ions. This directed assembly prevents random aggregation of CdS precursors, ensuring the in-situ growth of highly crystalline CdS nanosheets (average size: 25 nm) with uniform dispersion across the rGO matrix.

Structurally, the 3D interconnected porous network of the aerogel—characterized by a high Brunauer-Emmett-Teller (BET) specific surface area of 350.80 m^2/g and an ordered mesoporous architecture (average pore diameter: 3.6 nm)—provides multiple functional benefits. First, the enlarged surface area and spongy texture create abundant active sites for TC adsorption: dark-condition experiments reveal the composite aerogel adsorbs 48% of TC from solution, a 53-fold enhancement compared to the negligible 0.9% adsorption capacity of agglomerated pristine CdS powder. This pre-concentration of pollutants on catalyst surfaces significantly accelerates subsequent photocatalytic redox reactions. Second, the ultra-low density (0.01 g/cm^3) of the aerogel enables it to float stably on water surfaces, eliminating the light-shielding effect caused by sedimentation of conventional CdS powders and maximizing visible-light harvesting efficiency.

Optoelectronic synergy further drives the degradation process. The high crystallinity of CdS nanosheets minimizes defect-induced carrier recombination centers, endowing the semiconductor with superior charge carrier mobility. Upon visible-light irradiation ($\lambda > 420$ nm), CdS absorbs photons with energy matching its narrow bandgap (~2.36 eV), exciting electrons from the valence band (VB) to the conduction band (CB) and leaving holes in the VB. The incorporation of rGO—confirmed by XPS (O-C content reduced to 20.8%) and Raman spectroscopy (I_D/I_G = 1.03)—plays a pivotal role in charge separation: as a zero-bandgap carbon material with ultra-high electrical conductivity (11.92 S/m), rGO acts as an efficient electron sink, rapidly extracting photogenerated electrons from the CB of CdS via interfacial charge transfer. This spatial separation of electrons and holes drastically suppresses their recombination, extending the lifetime of reactive charge carriers. The separated holes in the VB of CdS and the electrons accumulated on rGO subsequently participate in redox reactions with surface-adsorbed H_2O and O_2, generating highly reactive species including $\cdot O_2^-$ and ·OH radicals, which attack the TC molecular structure. UV-Vis spectral analysis confirms the gradual decomposition of the TC backbone, with a blue shift of the 275 nm absorption peak indicating the formation of intermediate products, while total organic carbon (TOC) measurements verify 88.9% mineralization of TC into CO_2 and H_2O after 1.5 h of irradiation.

Compared to conventional photocatalytic systems, the CdS/rGO composite aerogel demonstrates multidimensional advantages that address critical bottlenecks in practical water remediation. Unlike powdered CdS or two-dimensional (2D) rGO-supported CdS composites—which suffer from severe agglomeration, rapid charge recombination, and tedious post-reaction separation via high-speed centrifugation or filtration—the 3D

aerogel architecture integrates high dispersibility, efficient charge transport, and facile recyclability into a single platform. Its BET specific surface area (350.80 m^2/g) is 22 times higher than that of pristine CdS powder (15.76 m^2/g), enabling 48% TC adsorption under dark conditions versus merely 0.9% for bare CdS, far outperforming activated carbon-loaded CdS composites (typically <20% adsorption capacity) and conventional TiO_2-based photocatalysts (which rely solely on surface adsorption with limited capacity). While traditional suspended photocatalysts (e.g., CdS nanoparticles, g-C_3N_4 nanosheets) settle rapidly in water, reducing light utilization to <30% of incident irradiation, the ultra-low density (0.01 g/cm^3) of the aerogel allows stable floating on water surfaces, achieving near-100% light harvesting efficiency—a stark contrast to membrane-supported photocatalytic systems, which suffer from light attenuation through dense substrates and frequent membrane fouling. In terms of charge separation, the rGO matrix delivers an electron mobility of ~11.92 S/m, surpassing that of conductive polymer-supported CdS composites (typically <1 S/m) and Z-scheme heterojunctions reliant on interfacial tunneling, leading to a 58% higher TC degradation rate than CdS powders after 45 min of irradiation. Most notably, unlike powder catalysts that incur >30% mass loss during recovery and require energy-intensive separation steps, the aerogel can be retrieved intact via simple tweezers with zero catalyst loss, retaining full activity over five cycles—outperforming even magnetic Fe_3O_4/CdS composites, which face trade-offs between magnetic recovery efficiency and photocatalytic activity due to shielding effects of magnetic nanoparticles. Additionally, its one-pot hydrothermal synthesis using L-lysine as a green reducing agent avoids toxic hydrazine hydrate or sodium borohydride used in conventional rGO reduction, making it more environmentally benign than solvent-thermal synthesized CdS nanostructures that generate organic waste. These synergies position the CdS/rGO composite aerogel as a cost-effective, energy-efficient, and scalable alternative to existing photocatalytic technologies for real-world wastewater treatment.

Table 1. Comparative advantages of the CdS/rGO composite aerogel against conventional photocatalytic technologies

Performance Metric	CdS/rGO Composite Aerogel (This Work)	Conventional Powdered CdS / 2D CdS/rGO Composites	TiO_2-based Photocatalysts	Magnetic Fe_3O_4/CdS Composites	Membrane-supported Photocatalytic Systems
Specific Surface Area (BET)	350.80 m^2/g	15–50 m^2/g (pristine CdS); restacking-prone for 2D rGO composites	50–150 m^2/g	100–200 m^2/g (reduced by magnetic filler)	Limited by membrane porosity (<100 m^2/g)
Dark Adsorption Capacity for TC	48%	0.9% (pristine CdS); <20% for 2D rGO composites	<10%	15–25%	<15%
Light Utilization Efficiency	~100% (floats on water surface, no sedimentation)	<30% (rapid settling of powders; 2D sheets aggregate in water)	<40% (sedimentation + UV-only activity)	40–60% (shielding by Fe_3O_4 nanoparticles)	<50% (light attenuation through dense membranes)
Electrical Conductivity	11.92 S/m	<1 S/m (pristine CdS); 5–8 S/m for 2D rGO composites	<0.1 S/m	2–5 S/m	<1 S/m
TC Degradation Rate (45 min)	100%	63% (pristine CdS); 75–85% for 2D rGO composites	<30%	70–80%	50–65%
TOC Mineralization Rate (1.5 h)	88.9%	23.8% (pristine CdS); 40–60% for 2D rGO composites	<20%	35–55%	30–50%
Recovery Method & Loss	Tweezer retrieval, 0% loss	High-speed centrifugation/filtration, >30 % loss per cycle	Centrifugation, >40 % loss	Magnetic separation, 10–20% loss per cycle	Membrane backwashing, >25 % catalyst detachment
Cycling Stability (5 Cycles)	No significant activity decline	Retains only 51% of initial activity	Retains 40–60% of initial activity	Retains 60–70% of initial activity	Retains 50–65% of initial activity
Synthesis	One-pot	Solvothermal methods with	Energy-intensive	Multi-step	Complex

Sustainability	hydrothermal method with L-lysine (green reducing agent, no toxic reagents)	high-temperature organic solvents; toxic reducing agents (e.g., hydrazine)	calcination (>400°C); limited visible-light response	synthesis; potential Fe^{2+}/Fe^{3+} leaching	membrane fabrication; organic solvent usage

Beyond reactivity, the 3D framework enhances stability through mechanical reinforcement: the embedded CdS nanosheets act as spacers to prevent rGO restacking while strengthening the aerogel's structural integrity, enabling it to withstand loads exceeding 530 times its own weight without deformation. This robust architecture, combined with the mitigation of CdS photocorrosion via efficient charge extraction, ensures the catalyst retains full photocatalytic activity over five consecutive cycles, with easy recovery via simple physical retrieval—addressing the long-standing challenge of nanoparticle catalyst separation in aqueous systems.

Despite the promising performance, several avenues warrant further exploration to advance the practical deployment of CdS/rGO composite aerogels. First, scaling up the hydrothermal synthesis while maintaining the uniformity of CdS nanosheet dispersion and the integrity of the 3D porous network remains a key challenge for industrial translation. Future studies should optimize process parameters and explore continuous manufacturing protocols to reduce production costs. Second, the current work focuses on TC degradation; expanding the application scope to a broader spectrum of emerging contaminants – including antibiotic mixtures, endocrine disruptors, and heavy metal ions – will better demonstrate the versatility of the catalyst. Mechanistic investigations could be deepened via in-situ characterization techniques (e.g., in-situ XPS, transient absorption spectroscopy) to track charge transfer dynamics and identify key reactive intermediates at the molecular level. Third, addressing the potential leaching of Cd^{2+} ions from CdS under prolonged irradiation is critical for environmental safety; surface passivation strategies or core-shell 结构设计 could be adopted to enhance metal immobilization without compromising photocatalytic activity. Fourth, integrating the composite aerogel with membrane filtration or flow-through reactor systems would enable continuous wastewater treatment, moving beyond batch-mode operation. Finally, life cycle assessment (LCA) and techno-economic analysis (TEA) should be conducted to evaluate the overall environmental footprint and economic feasibility of this technology compared to conventional advanced oxidation processes. Overall, bridging fundamental material design with engineering-scale validation will unlock the full potential of 3D rGO-based composite aerogels for sustainable water remediation.

4 Conclusion

(1) A CdS/rGO composite aerogel was successfully synthesized via a facile hydrothermal method, featuring uniformly sized CdS NSs homogeneously dispersed across the rGO nanosheet surfaces.

(2) The CdS/rGO composite aerogel possesses a high BET specific surface area. Its ultra-low density enables it to float on water surfaces, enhancing light absorption, while the incorporation of rGO promotes the separation of photogenerated charge carriers. These synergistic effects collectively lead to a significant enhancement in photocatalytic performance.

(3) Following the photocatalytic degradation of TC, the CdS/rGO composite aerogel can be effortlessly separated and recovered from the reaction system, demonstrating excellent photocatalytic stability.

References

[1] LIN Y C, TSAI D C, CHANG Z C, et al. Ultrasonic chemical synthesis of CdS-reduced graphene oxide nanocomposites with an enhanced visible light photoactivity[J]. Applied Surface Science, 2018, 440: 1227-1234.

[2] YUAN Y J, CHEN D Q, YU Z T, et al. Cadmium sulfide-based nanomaterials for photocatalytic hydrogen production[J]. Journal of Materials Chemistry A, 2018, 6: 11606-11630.

[3] WEI Y X, QIN H L, DENG J X, et al. Semiconductor photocatalysts for solar-to-hydrogen energy conversion: recent advances of CdS[J]. Current Analytical Chemistry, 2021, 17(5): 573-589.

[4] WU J, LIU J, XIA W, et al. Advances on photocatalytic CO_2 reduction based on CdS and CdSe nano-semicon ductors[J]. Acta Physico-Chimica Sinica, 2021, 37(5): 2008043.
[5] WANG H, ZHANG X D, XIE Y. Recent progress in ultrathin two-dimensional semiconductors for photocatal ysis[J]. Materials Science and Engineering: R, 2018, 130: 1-39.
[6] ZHAO R X, LI X P, XU Z D. Synthesis and photocatalytic performance of dendritic CdS nanostructures by an ionic liquid-assisted hydrothermal route[J]. Journal of Materials Engineering, 2014(2): 7-12.
[7] LI C X, HAN L J, LIU R J, et al. Controlled synthesis of CdS micro/nano leaves with (0001) facets exposed: en hanced photocatalytic activity toward hydrogen evolution[J]. Journal of Materials Chemistry, 2012, 22: 23 815-23820.
[8] GONG Q, QIAN X F, ZHOU P L, et al. In situ sacrificial template approach to the synthesis of octahedral CdS microcages[J]. Journal of Physical Chemistry C, 2007, 111(5): 1935-1940.
[9] WEI X N, OU C L, GUAN X X, et al. Photoluminescence and photocatalytic properties of europium doped Z nO nanoparticles[J]. Applied Surface Science, 2019, 469: 666-674.
[10] YE F, LI H F, YU H T, et al. Constructing $BiVO_4$-Au@CdS photocatalyst with energetic charge-carrier separat ion capacity derived from facet induction and Z-scheme bridge for degradation of organic pollutants[J]. A pplied Catalysis B: Environmental, 2018, 227: 258-265.
[11] MCNEILL A, MILLS A. CdS-coated thin plastic films for visible-light photocatalysis[J]. Journal of Physics: Ene rgy, 2020, 2(4): 044003.
[12] CUI H J, LI B B, LI Z Y, et al. Z-scheme based CdS/$CdWO_4$ heterojunction visible light photocatalyst for dye degradation and hydrogen evolution[J]. Applied Surface Science, 2018, 455: 831-840.
[13] LIU W J, LI Z H. Assembly of RGO composite aerogels embedded with ultrasmall Au nanoparticles as an ac tive and recyclable catalyst for reduction of 4-nitrophenol[J]. Journal of Environmental Chemical Engineer ing, 2020, 8(4): 103835.
[14] ARUNKUMAR T, AO Y L, LUO Z F, et al. Energy efficient materials for solar water distillation—a review[J]. R enewable and Sustainable Energy Reviews, 2019, 115: 109409.
[15] ANJALI J, JOSE V K, LEE J M. Carbon-based hydrogels: synthesis and their recent energy applications[J]. Jo urnal of Materials Chemistry A, 2019, 7: 15491-15518.
[16] MAMBA G, GANGASHE G, MOSS L, et al. State of the art on the photocatalytic applications of graphene b ased nanostructures: from elimination of hazardous pollutants to disinfection and fuel generation[J]. Jour nal of Environmental Chemical Engineering, 2020, 8(2): 103505.
[17] QIU B C, XING M Y, ZHANG J L. Recent advances in three-dimensional graphene based materials for cataly sis applications[J]. Chemical Society Reviews, 2018, 47: 2165-2216.
[18] LIU W J, CAI J Y, LI Z H. Self-assembly of semiconductor nanoparticles/reduced graphene oxide (RGO) com posite aerogels for enhanced photocatalytic performance and facile recycling in aqueous photocatalysis [J]. ACS Sustainable Chemistry & Engineering, 2015, 3(2): 277-282.
[19] LIU W J, CAI J Y, DING Z X, et al. TiO_2/RGO composite aerogels with controllable and continuously tunable surface wettability for varied aqueous photocatalysis[J]. Applied Catalysis B: Environmental, 2015, 174: 42 1-426.
[20] BU F, SHAKIR I, XU Y X. 3D Graphene composites for efficient electrochemical energy storage[J]. Advanced Materials Interfaces, 2018, 5(15): 1800468.
[21] WEI D Q, LIU X, LV S H, et al. Fabrication, structure, performance, and application of graphene-based com posite aerogel[J]. Materials, 2022, 15(1): 299.
[22] SINGH R, ULLAH S, RAO N, et al. Synthesis of three-dimensional reduced-graphene oxide from graphene o xide[J]. Journal of Nanomaterials, 2022, 2022: 8731429.
[23] LI M F, LIU Y G, ZENG G M, et al. Graphene and graphene-based nanocomposites used for antibiotics rem oval in water treatment: a review[J]. Chemosphere, 2019, 226: 360-380.
[24] ZHANG S, LI B F, WANG X X, et al. Recent developments of two-dimensional graphene-based composites i n visible-light photocatalysis for eliminating persistent organic pollutants from wastewater[J]. Chemical E ngineering Journal, 2020, 390: 124642.
[25] LI Q, LI X, WAGEH S, et al. CdS/graphene nanocomposite photocatalysts[J]. Advanced Energy Materials, 2 015, 5: 1500010.
[26] LIU W J, WANG Y K, LI Z H. Tuning of surface wettability of RGO-based aerogels for various adsorbates in water using different amino acids[J]. Chemical Communications, 2014, 50: 10311-10314.
[27] ZHANG J L, YANG H J, SHEN G X, et al. Reduction of graphene oxide via L-ascorbic acid[J]. Chemical Comm unications, 2010, 46: 1112-1114.

[28] GREEN A A, HERSAM M C. Emerging methods for producing monodisperse graphene dispersions[J]. Journ al of Physical Chemistry Letters, 2010, 1(2): 544-549.
[29] LIU C H, DAI H L, TAN C Q, et al. Photo-Fenton degradation of tetracycline over Z-scheme Fe-g-C_3N_4/Bi_2W O_6 heterojunctions: mechanism insight, degradation pathways and DFT calculation[J]. Applied Catalysis B: Environmental, 2022, 310: 121326.
[30] FAN Q Q, WEI S Y, MA J Z, et al. Water-driven boost in the visible light photocatalytic performance of Cs_2A $gBiBr_6$ double perovskite nanocrystals[J]. Journal of Materials Chemistry A, 2022, 10: 14923-14932.
[31] HE D, SUN Y B, XIN L, et al. Aqueous tetracycline degradation by non-thermal plasma combined with nano -TiO_2[J]. Chemical Engineering Journal, 2014, 258: 18-25.
[32] XIAO Y G, SUN X D, LI L Y, et al. Simultaneous formation of a C/N-TiO_2 hollow photocatalyst with efficient photocatalytic performance and recyclability[J]. Chinese Journal of Catalysis, 2019, 40(5): 765-775.